The BG21 Isoform of Golli Myelin Basic Protein Is Intrinsically Disordered with a Highly Flexible Amino-Terminal Domain†

Mumdooh A. M. Ahmed,‡ Vladimir V. Bamm,§ George Harauz,*,§ and Vladimir Ladizhansky*,‡

Departments of Physics and Molecular and Cellular Biology, and Biophysics Interdepartmental Group, University of Guelph, 50 Stone Road East, Guelph, Ontario N1G 2W1, Canada

Received April 3, 2007; Revised Manuscript Received May 30, 2007

ABSTRACT: The genes of the oligodendrocyte lineage (Golli) encode a family of developmentally regulated isoforms of myelin basic protein. The "classic" MBP isoforms arise from transcription start site 3, whereas Golli-specific isoforms arise from transcription start site 1, and comprise both Golli-specific and classic MBP sequences. The Golli isoform BG21 has been suggested to play roles in myelination and T cell activation pathways. It is an intrinsically disordered protein, thereby presenting a large effective surface area for interaction with other proteins such as Golli-interacting protein. We have used multidimensional heteronuclear NMR spectroscopy to achieve sequence-specific resonance assignments of the recombinant murine BG21 in physiologically relevant buffer, to analyze its secondary structure using chemical shift indexing (CSI), and to investigate its backbone dynamics using ^{15}N spin relaxation measurements. We have assigned 184 out of 199 residues unambiguously. The CSI analysis revealed little ordered secondary structure under these conditions, with only some small fragments having a slight tendency toward α-helicity, which may represent putative recognition motifs. The ^{15}N relaxation and NOE measurements confirmed the general behavior of the protein as an extended polypeptide chain, with the N-terminal Golli-specific portion (residues S5−T69) being exceptionally flexible, even in comparison to other intrinsically disordered proteins that have been studied this way. The high degree of flexibility of this N-terminal region may be to provide additional plasticity, or conformational adaptability, in protein−protein interactions. Another highly mobile segment, A126-S127-G128-G129, may function as a hinge.

The genes of the oligodendrocyte lineage (Golli)[1] give rise to several isoforms of the myelin basic protein (MBP) family (*1*−*3*). The classic isoforms of MBP arise from transcription start site 3 and are expressed primarily in the mature central nervous system, where they are known to maintain the compaction of the myelin sheath (*1*). These proteins are also candidate self-antigens in the autoimmune disease multiple sclerosis (*3*−*6*). The Golli isoforms arise from transcription start site 1 and have some structural elements in common with classic MBP but are more ubiquitously expressed in neurons and oligodendrocytes during embryonic development or differentiation, in specific subsets of neurons, in the immune system (spleen and thymus), and in olfactory brain regions (*7*−*11*).

It has been suggested that Golli MBPs might have roles in myelin elaboration in the central nervous system, during development and in remyelination attempts (*12*, *13*). They are also thought to participate in controlling Ca^{2+} influx in T cells (*14*). Studies of mice in which the Golli-specific portion of the gene was knocked out suggested that the Golli MBPs may be involved in suppression of a T cell activation pathway (*3*, *15*). The Golli MBPs are substrates for protein kinase C (PKC) and inhibit PKC activation pathways in T and probably also neuronal cells (*3*, *16*). This last function was suggested by the findings of yeast two-hybrid assays that showed a binding partner called Golli-interacting protein (GIP) (*17*), a phosphatase that acts on the carboxy-terminal domain of the largest subunit of RNA polymerase II and that is found in the nuclei of neuronal cells. It was suggested that GIP may be part of a transcriptional regulatory complex, modulating genes regulated by LIM family members (Lin-11/Isl-1/Mec-3, homeodomains with a common Zn^{2+}-binding motif) (*17*) and may function in silencing neuronal genes (*18*, *19*). Further insights into the biological importance of Golli MBPs can be obtained from structural characterization

† This work was supported by the Canadian Institutes of Health Research (CIHR, Operating Grant MOP 74468) and the Natural Sciences and Engineering Research Council of Canada (NSERC). V.L. is a Canada Research Chair holder and is a recipient of an Early Researcher Award from the Ontario Ministry of Research and Innovation. M.A.M.A. is a recipient of a Doctoral Studentship from the Ministry of Higher Education and Scientific Research of Egypt.

* To whom correspondence should be addressed. G.H.: e-mail, gharauz@uoguelph.ca; fax, 519-837-1802; telephone, 519-824-4120 ext 52535. V.L.: e-mail, vladimir@physics.uoguelph.ca; fax, 519-836-9967; telephone, 519-824-4120 ext 53989.

‡ Department of Physics and Biophysics Interdepartmental Group, University of Guelph.

§ Department of Molecular and Cellular Biology and Biophysics Interdepartmental Group, University of Guelph.

[1] Abbreviations: Golli, genes of the oligodendrocyte lineage; LIM, *L*in-11/*I*sl-1/*M*ec-3 domain; BG21, murine Golli-MBP isoform; rm-BG21, recombinant murine BG21; GIP, Golli-interacting protein; DSS, 2,2-dimethyl-2-silapentane-5-sulfonic acid; ddH_2O, distilled, deionized water; CD, circular dichroism spectroscopy; COSY, correlation spectroscopy; HSQC, heteronuclear single-quantum coherence; NOE, nuclear Overhauser effect; NOESY, nuclear Overhauser effect spectroscopy; CPMG, Carr−Purcell−Meiboom−Gill; CARA, computer-aided resonance assignment; CSI, chemical shift index; ppm, parts per million.

10.1021/bi700632x CCC: $37.00
Published on Web 08/04/2007

of these proteins, alone or with their interacting partners like GIP.

On the basis of their net charge to mean hydrophobicity ratio, and various spectroscopic measurements, all known forms of MBP (both classic and Golli) belong to the class of intrinsically disordered proteins (IDPs) (*1*, *20*). Many intrinsically disordered proteins are multifunctional and/or involved in signaling pathways. They have an extended conformation to present a large effective surface area for interaction with a variety of diverse ligands, all of which they bind with high specificity, and are often hubs of protein interaction networks (*21*, *22*).

The most powerful approach to probing the conformational dynamics and interactions of intrinsically disordered proteins is nuclear magnetic resonance (NMR) spectroscopy (*23*, *24*). Recent advances in NMR technology have allowed full assignments of backbone resonances of partially folded and unfolded proteins and have also shed light onto the structure and dynamics of those proteins by the use of parameters such as chemical shifts, scalar coupling constants, and temperature coefficients (*23*, *25*). The deviation of chemical shifts of many spins, including $^{13}C^{\alpha}$, $^{13}C^{\beta}$, $^{13}C'$, and $^{1}H^{\alpha}$ from random coil values, provides a sensitive probe of secondary structure propensities (*26*, *27*). The measurement of ^{15}N and ^{13}C spin relaxation rates provides information about internal dynamics of proteins on the picosecond to nanosecond and microsecond to millisecond time scales (*25*, *28*, *29*).

In this study, multidimensional heteronuclear NMR spectroscopy was used to achieve sequence-specific resonance assignments of the 21.6 kDa recombinant murine Golli-MBP isoform (rmBG21) and the analysis of its secondary structure using chemical shift indexing (CSI) and of ^{15}N spin relaxation measurements to investigate its backbone dynamics. This is the first step toward studies of rmBG21's interactions with other proteins such as GIP.

MATERIALS AND METHODS

Materials. Most chemicals were of reagent grade and were acquired from either Fisher Scientific (Unionville, Ontario, Canada) or Sigma-Aldrich (Oakville, Ontario, Canada). Electrophoresis grade chemicals were purchased from ICN Biomedicals (Costa Mesa, CA) or Bio-Rad Laboratories (Mississauga, Ontario, Canada). The Ni^{2+}-NTA (nitrilotriacetic acid) agarose beads were purchased from Qiagen (Mississauga, Ontario, Canada). The stable isotopic compounds D_2O, $^{15}NH_4Cl$, and [$^{13}C_6$]glucose were obtained from Cambridge Isotope Laboratories (Andover, MA).

Sample Preparation. The 21.6 kDa recombinant murine BG21 (rmBG21) was expressed in *Escherichia coli*, grown in M9 minimal media supplemented with [^{13}C]glucose and $^{15}NH_4Cl$, and purified as previously described (*30*). All measurements were done on a single 1 mM protein sample in 100 mM KCl and 90% H_2O/10% D_2O, pH 6.9 ± 0.1. An amount of 0.005% NaN_3 was added to inhibit bacterial growth.

Chemical Shift Assignments. All of the NMR experiments were recorded on a Bruker Avance spectrometer operating at a proton Larmor frequency of 600.13 MHz. All resonance assignments were done at 7 °C. Sequential connectivities of backbone resonances of all residues but prolines were established using the standard Bruker suite of 3D heteronuclear experiments: HNCO (*31*−*33*), HN(CA)CO (*32*, *34*), HNCACB (*35*, *36*), CBCA(CO)NH (*35*, *37*), and HBHA(CBCACO)NH (*35*, *37*). The relevant acquisition parameters for the different spectra are summarized in the Supporting Information.

Sequential connectivities of backbone resonances through prolyl residues were established using HACAN (*38*, *39*) at 7 °C. For the purpose of spin system identification, both HNCACB and HBHA(CBCACO)NH were utilized. All spectra were processed using NMRPipe (*40*). A Lorentz-to-Gauss window function was applied in all dimensions with proper line broadening. The time domains were zero-filled up to 1024 × 1024 × 4096 complex points in the $F_1 \times F_2 \times F_3$ dimensions, respectively, prior to Fourier transformation. The ^{1}H chemical shifts were referenced directly to 2,2-dimethyl-2-silapentane-5-sulfonic acid (DSS), while the ^{15}N and ^{13}C chemical shifts were referenced indirectly to DSS (*41*). The two-dimensional $^{15}N-^{1}H$ heteronuclear single-quantum coherence (HSQC) (*42*−*45*) spectra were acquired as a function of temperature to assist in the analysis and interpretation of the heteronuclear 3D data at 27 °C. The $^{15}N-^{1}H$ HSQC spectra were measured at 7, 11, 15, 19, 23, and 27 °C, and the gradual change of positions of cross-peaks already assigned at 7 °C was followed.

Backbone Resonance Assignments. All spin systems were created on the basis of ^{13}C, ^{15}N, and ^{1}H ppm values of $^{13}C'[i-1]$, $^{15}N[i]$, and $^{1}H^{N}[i]$ of each system in the HNCO spectrum. The spins were picked and assigned using CARA (*46*) and an in-house script written in LUA (www.lua.org) and executed using the built-in LUA interpreter. All other spins, $C^{\alpha}[i]$, $C^{\alpha}[i-1]$, $C^{\beta}[i]$, $C^{\beta}[i-1]$, $C'[i]$, and H^{α}, were picked and partially assigned automatically using another set of in-house LUA scripts. The remaining unassigned spins were identified manually. Most of the sequence-specific connectivities were established using AUTOLINK (*47*). The remaining assignments were obtained manually using iterative trials.

Secondary Chemical Shifts. The chemical shift deviations were used to assess the secondary structure propensities along the backbone of rmBG21. Random coil values (*48*) were corrected for sequence dependence using sequence-specific correction factors determined for a set of Ac-GGXGG-NH_2 peptides in 8 M urea at pH 2.3 (*49*). The normalized sequence corrected chemical shift indexes $\Delta\delta C^{\alpha}$, $\Delta\delta C^{\beta}$, $\Delta\delta N$, and $\Delta\delta H^{N}$ for C^{α}, C^{β}, N, and H^{N}, respectively, were combined to yield a normalized chemical shift index:

$$CSI_N = \frac{1}{2}\left\{[\Delta\delta C^{\alpha}]_N - \frac{1}{3}([\Delta\delta C^{\beta}]_N + [\Delta\delta N]_N + [\Delta\delta H^{N}]_N)\right\} \quad (1)$$

^{15}N Relaxation Measurements. The relaxation parameters of ^{15}N were measured using standard approaches (*50*−*52*). The spin−spin relaxation constant R_2 measurements were done with Carr−Purcell−Meiboom−Gill (CPMG) (*53*) delays of 0, 64, 128, 160, 192, 224, 256, 288, and 320 ms. The relaxation rate was determined from the decay of the intensity of each $^{15}N-^{1}H$ cross-peak in this series of spectra. The R_1 (*51*, *52*) rate measurements were conducted with relaxation delays of 1.6, 50, 100, 200, 300, 400, 800, 1000, and 1200 ms. All of the relaxation parameters along with the $^{15}N-\{^{1}H\}$ NOE constant for backbone ^{15}N nuclei were

measured at 7 and 27 °C, at a field strength of 600.13 MHz, and with 38 transients per point. The relaxation constants and the experimental errors were extracted by a single exponential curve fitting of the peak heights using the SPARKY (T. D. Goddard and D. G. Kneller, SPARKY 3, University of California, San Francisco) built-in option. The best fit was obtained by minimizing the root-mean-square (RMS) deviation of the experimental peak heights from the fit. Random errors for R_1 and R_2 values were estimated by calculating a best fit for a set of perturbed heights 5000 times; the heights were perturbed by computer-simulated noise with a Gaussian distribution of zero mean and with variance equal to the root-mean-square deviation of the original heights from the original best fit. The spread in the best fit values was used as a measure of the experimental random error.

The steady-state $\{^1H\}-^{15}N$ NOE constants were obtained from the ratio I_{NOE}/I_{NONOE}, where I_{NOE} and I_{NONOE} are the peak heights in the NOE spectra with and without proton saturation, respectively. The spectra were collected using a standard experiment described elsewhere (*51*), with the same acquisition parameters as those of the HSQC spectrum, except that the number of transients per point was 192. The uncertainty in measuring NOE constants was determined using the relation:

$$\sigma_{NOE} = \frac{I_{NOE}}{I_{NONOE}}\left[\left(\frac{\sigma_{INOE}}{I_{NOE}}\right)^2 + \left(\frac{\sigma_{INONOE}}{I_{NONOE}}\right)^2\right]^{1/2} \qquad (2)$$

where σ_{INOE} and σ_{INONOE} are the white level noise of both spectra with and without proton saturation, respectively. Those noise levels were evaluated as the RMS intensity of a region free of any peaks, using an in-house LUA script executed using the built-in LUA interpreter in CARA (*46*).

RESULTS AND DISCUSSION

NMR Resonance Assignments. Uniformly ^{13}C,^{15}N-labeled rmBG21 dissolved in water with 10% D_2O, 100 mM KCl, and 0.005% sodium azide at pH 6.9 ± 0.1 was used for the multidimensional NMR studies. The sample was found to be very stable (as judged by criteria such as the undiminished NMR signal intensity) for at least 1 year in these solvent conditions and in a wide range of temperatures from 7 to 37 °C. Whereas the classic MBP isoforms are primarily membrane-associated in vivo, justifying the use of membrane-mimetic solvents and other such conditions (*1*, *54*), the Golli protein is not necessarily lipid-associated in the cell. Thus, the solution condition used here for rmBG21 was chosen as being simple yet still physiologically relevant, especially for future protein−protein interaction studies. In contrast to membrane-associated proteins, we have never observed BG21 to have a propensity to aggregate in solution (*30*).

Residue types were identified by using aliphatic ^{13}C chemical shifts from a combination of HNCACB and HBHA(CBCACO)NH experiments. Because of the low degree of ordered secondary structure, the chemical shifts in intrinsically disordered proteins such as BG21 are poorly dispersed compared to classically folded ones. The spins whose chemical shifts are most affected by this property are C^α, C^β, H^α, and H^N. Consequently, the C^α, C^β, H^α, and H^N chemical shifts for the same residue type tend to be degenerate (*55*). Spin system overlap and degeneracy make it difficult to use the standard methodology for assignment, pioneered by Wüthrich and co-workers (*56*). In contrast, the chemical shifts of the backbone carbonyl carbon ($^{13}C'$) and amide nitrogen atoms (^{15}N) are much less structure-dependent, but much more sequence-dependent (*25*, *55*, *57*). Thus, our sequential assignment strategy relied heavily on the use of CO-based triple-resonance experiments, HN(CA)CO and HNCO, and was assisted by C^α-based CBCA(CO)HN and HNCACB triple-resonance experiments.

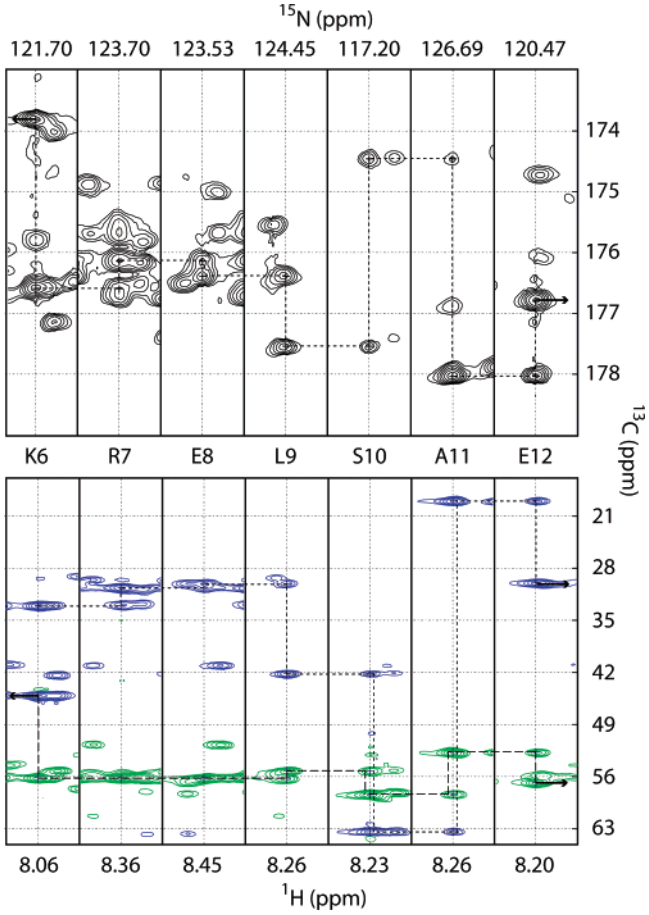

FIGURE 1: Strip plots extracted from three-dimensional heteronuclear NMR experiments for backbone assignment. Inter- and intraresidue correlations were obtained from the HN(CA)CO spectrum (top), correlating the $H^N[i]$ and N[*i*] with C′[*i*] and C′[*i* − 1] resonances, and from the HNCACB spectrum (bottom), correlating $H^N[i]$ and N[*i*] with $C^\alpha[i]$, $C^\alpha[i-1]$, $C^\beta[i]$, and $C^\beta[i-1]$ resonances. Both experiments were recorded at 7 °C. Connectivities between residues K6 and E12 of rmBG21 are shown.

As an example, parts of the HN(CA)CO and HNCACB spectra used for backbone assignments are shown in Figure 1. Out of a total of 199 residues, 184 residues were assigned unambiguously. The assignments of eight other residues, N2, N86, G5, G188, K6, K189, E24, and E47, were ambiguous due to sequence similarity and the disordered nature of the protein, which resulted in identical chemical shifts for corresponding spins. The first two residues, N2 and N86, are parts of the sequence-similar fragments G1-N2-H3 and G85-N86-R87, respectively. Likewise, the glutamyl residues E24 and E47 are found in the middle of similar triplet fragments: G23-E24-A25 and G46-E47-A48. Finally, the G5-K6 and G188-K189 pairs are found in the similar fragments S4-G5-K6-R7 and S187-G188-K189-V190. The remaining seven unassigned residues included R164, D170, and five histidyl residues belonging to the His_6 tag (H195−H199), which could not be assigned because of the spin system overlap in the HSQC spectra. The assigned ^1H, ^{13}C,

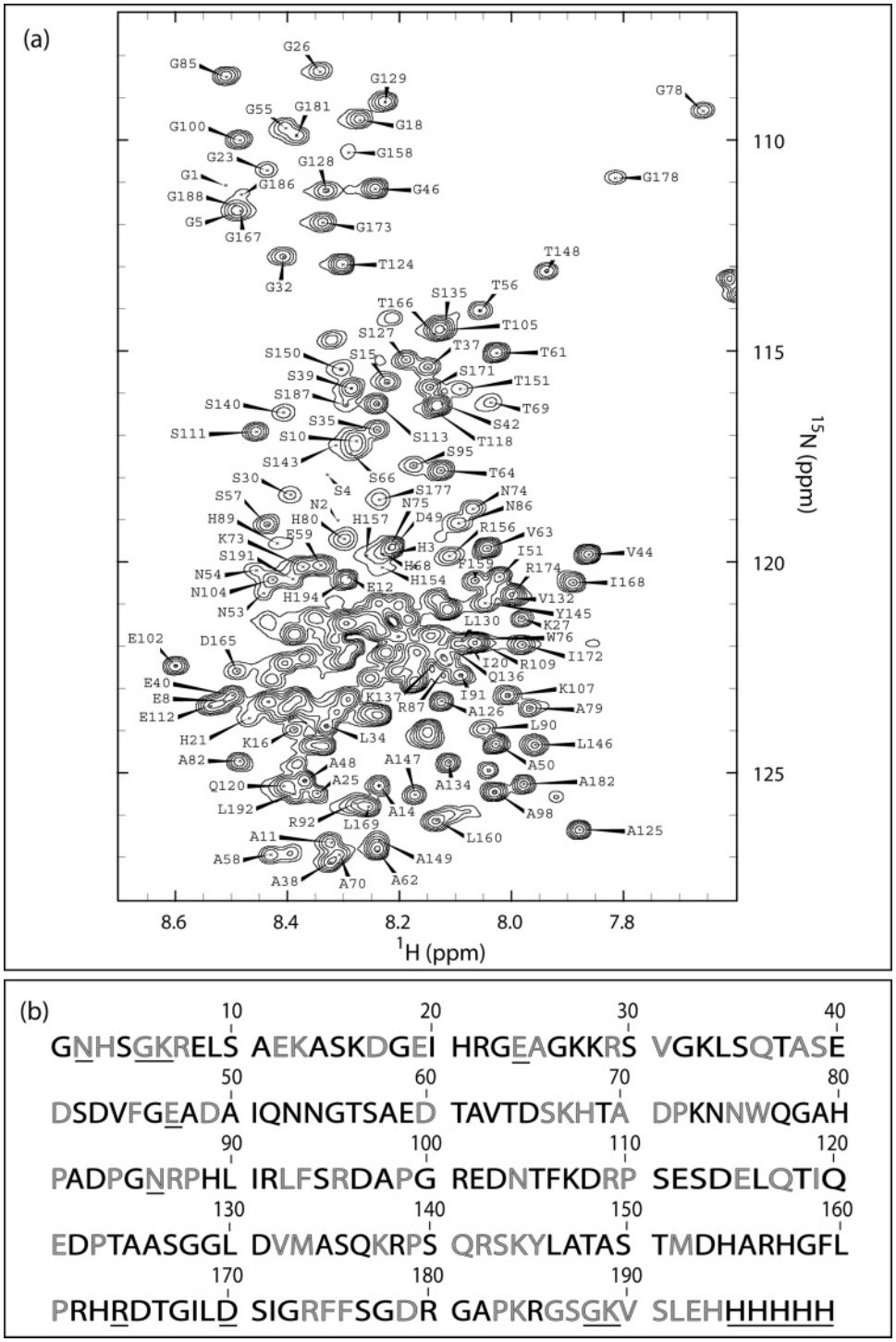

FIGURE 2: (a) Two-dimensional ^{1}H−^{15}N HSQC spectrum of rmBG21 at 27 °C, with backbone resonance assignments of most resolved non-prolyl resonances. (b) Amino acid sequence of rmBG21. Assigned residues, which are resolved in the HSQC spectrum, are shown in black. Residues assigned, but not resolved in the HSQC spectrum, and prolyl residues are shown in gray. Ambiguously assigned residues are shown in gray and underlined. Unassigned residues are shown in black and underlined.

and ^{15}N chemical shifts at 7 °C have been deposited in the BioMagResBank database (http://www.bmrb.wisc.edu) with accession number 7358.

To follow possible temperature dependence of the secondary structure (*58*−*64*), and to facilitate the temperature-dependent relaxation studies discussed below, the assignments of cross-peaks in the ^{1}H−^{15}N HSQC spectrum were extended to 27 °C by simply monitoring the gradual change of the cross-peak positions in the range between 7 and 27 °C. The peaks that overlapped in the HSQC spectrum were reassigned with the assistance of the 3D CBCA(CO)-NH correlation experiment. The same experiment was used to obtain assignments of C^{α} and C^{β} chemical shifts at 27 °C. The peaks did not undergo significant shifts in the carbon dimension: the positions of the C^{α} resonances shifted by up to 0.696 ppm with a mean of 0.261 ppm, whereas the C^{β} lines shifted by up to 0.445 ppm.

To map the pH dependence of the spectra, a set of 2D ^{1}H−^{15}N HSQC spectra were collected at different pH values in the range 5.6−10 (not shown). Spectra of rmBG21 at pH

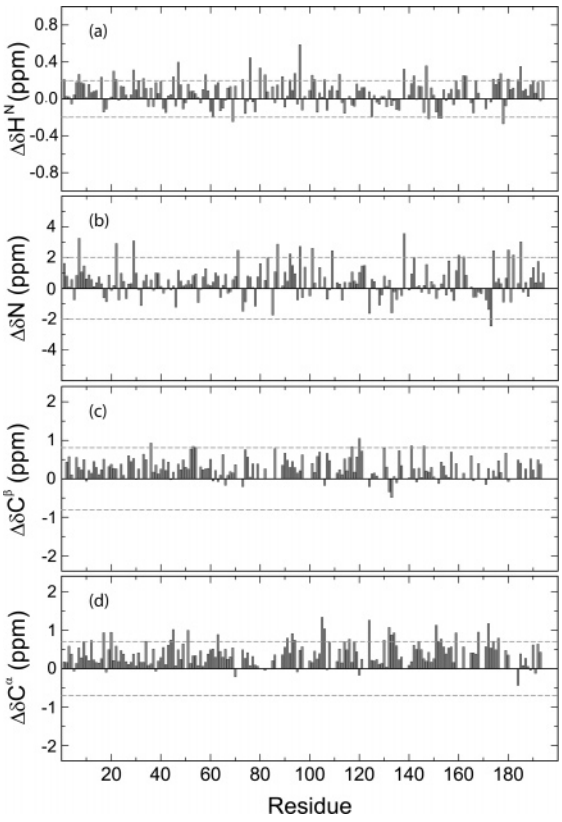

FIGURE 3: Chemical shift difference index plots of H^N (a), N (b), C^β (c), and C^α (d). The random coil values for H^N, N, and C^α have been adjusted for sequence dependence (corrections for C^β are not available). The reference lines in these plots correspond to threshold values at which differences begin to reflect regions of possible ordered secondary structure formation (*29*).

higher than 8.0 lacked many cross-peaks due to fast exchange of amide protons (*65*). The dispersion of the HSQC spectra at pH values in the range of 5.6−8 indicated that the protein remained unstructured. Oligodendrocytes have been shown to have intracellular pH microdomains, discrete regions differing from the surrounding cytoplasm by >0.1 pH unit (*66*). It would be expected that such pH variations alone would not have a significant effect on the conformation of BG21 in vivo.

Figure 2a shows the $^1H-^{15}N$ HSQC spectrum of rmBG21 taken at 27 °C, along with spectral assignments. The chemical shift dispersions of ^{15}N (∼20 ppm) and especially of $^1H^N$ (∼0.9 ppm) were largely independent of temperature in the probed temperature range and are typical for strongly unfolded proteins, e.g., for denatured ubiquitin (*67*). At all temperatures, the cross-peaks in the HSQC spectra are separated into regions typical of the residue random coil positions (G, S/T, other backbone amides), in line with our previous circular dichroism (CD) spectroscopy studies of rmBG21 demonstrating that it has an extended conformation under normal conditions (*30*). Overall, a total of 120 residues out of the unambiguously assigned 174 non-prolyl residues were resolved in the $^1H-^{15}N$ HSQC plane and could be used for site-specific analysis of the molecule. The residues corresponding to these 120 peaks are uniformly distributed along the protein amino acid sequence as shown in Figure 2b. Thus, the $^1H-^{15}N$ HSQC spectrum can be considered to be representative of the entire protein's behavior, e.g., in relaxation studies as explained below.

Secondary Chemical Shifts. The deviations of chemical shifts of $^{13}C^\alpha$, $^{13}C^\beta$, $^{13}C'$, and $^1H^\alpha$ from random coil values provide a sensitive amino acid-specific probe for secondary structure propensities. Both theoretical calculations and

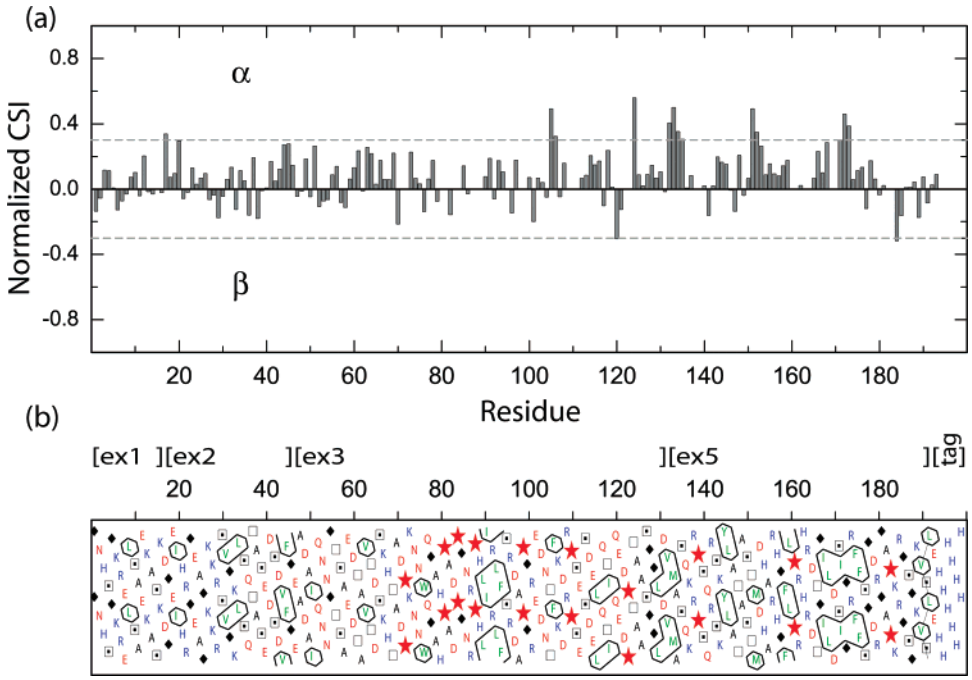

FIGURE 4: (a) Overall normalized chemical shift difference index. The reference line corresponds to an approximate threshold value at which the CSIs start to reflect regions of ordered secondary structure. This threshold value has been estimated from eq 1 along with the reference values in Figure 3. (b) Hydrophobic cluster analysis (HCA) plot of rmBG21. Four amino acids are represented here by special symbols (□, threonine; ⊡, serine; ◆, glycine; ★, proline). The visual enhancement is achieved by the use of the following colors: green for hydrophobic residues (V, L, I, F, W, M, Y), red for "acidic" (D, E, N, Q) and prolyl (P) residues, blue for "basic" residues (H, K, R), and black for other residues (G, S, T, C, A). Sets of adjacent hydrophobic residues are contoured and named hydrophobic clusters. The top bar of panel b shows the different exons of the gene encoding rmBG21: exons 1−3 are Golli-specific exons, and exon 5 is the classic exon.

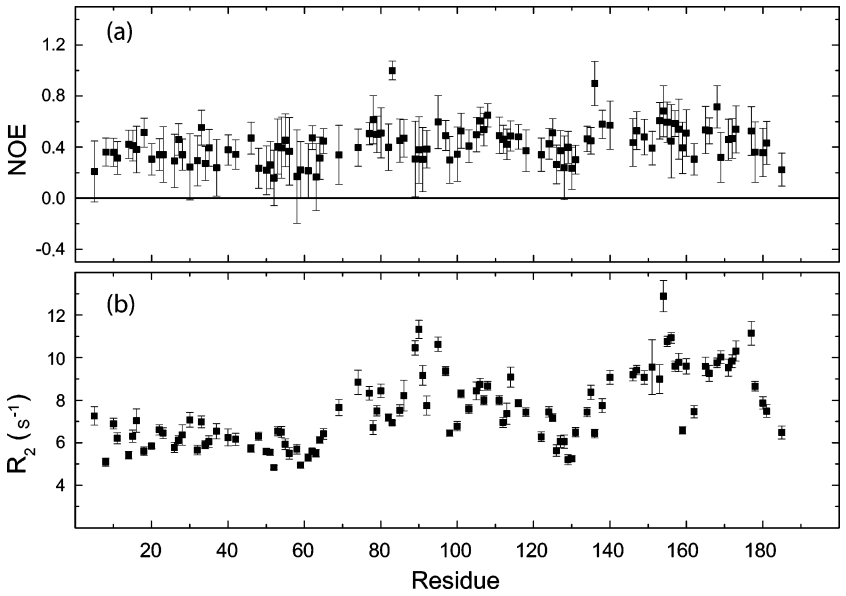

FIGURE 5: Relaxation measurements of rmBG21 at 7 °C and at 600 MHz field strength: (a) heteronuclear $\{^1H\}-^{15}N$ NOE values; (b) R_2 values.

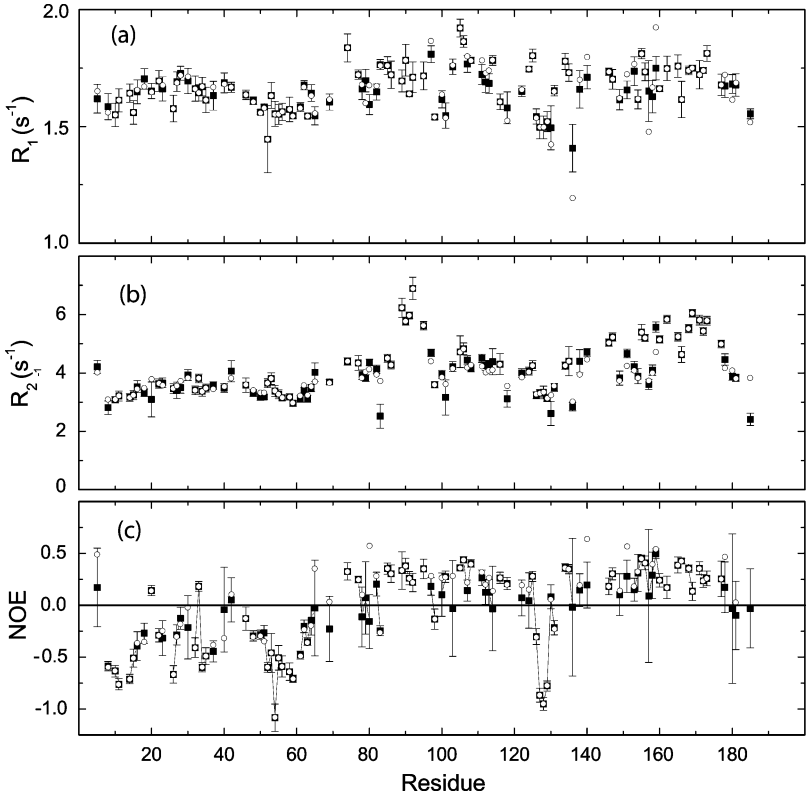

FIGURE 6: Experimental relaxation measurements of rmBG21 at 27 °C and at 600 MHz field strength (■) and MODELFREE best fit values (○): (a) R_1 values; (b) R_2 values; (c) heteronuclear $\{^1H\}-^{15}N$ NOE values.

empirical analyses have shown that these resonances are reliable indicators of secondary structure (*27*, *68*). In α-helices, both $^{13}C^{\alpha}$ and $^{13}C'$ are shifted downfield relative to their random coil values, whereas $^{13}C^{\beta}$ and $^{1}H^{\alpha}$ are shifted upfield. In β-strands, $^{13}C^{\alpha}$ and $^{13}C'$ are shifted upfield, and $^{13}C^{\beta}$ and $^{1}H^{\alpha}$ are shifted downfield relative to their random coil values (*23*, *25*, *27*, *68*). The combined use of these secondary shifts gives more precise definition of secondary structure boundaries than the use of single spin shifts alone (*23*, *25*, *27*, *68*). Although sequence-based predictions of rmBG21 indicate the potential presence of some α-helices in the fragments R7−A14, K27−Q36, S42−I51, D114−Q120, T124−S135, and K144−R156 (*30*) [and fragments L130−S135 and I168−F175 based on the YASPIN prediction method (*69*)], a conventional multinuclear chemical shift indexing (*68*) suggests here that the whole protein exists in a random coil conformation under our solution conditions at both temperatures examined, 7 and 27 °C. The sequence-corrected (*49*) chemical shift indexing of individual nuclei shown in Figure 3 indicates that the majority of the resonances are in the random coil range, except for a minor number of residues scattered along the sequence that have

deviations corresponding to α-helix or β-strand, but not in very extensive runs (*29*, *68*). For example, the C^{β} shifts show some weak tendency toward formation of β-strands, whereas both amide nitrogen and proton deviations display a combination of both possibilities for different fragments of the protein.

To get a more consistent picture of residual secondary structure in rmBG21, the shifts of $^{13}C^{\alpha}$, $^{13}C^{\beta}$, $^{1}H^{N}$, and ^{15}N were combined to yield a normalized chemical shift index plot, shown in Figure 4a. Most of the protein exists in the random coil conformation except for minor fragments around V132−S135, T151−D153, and S171−G173, which show a slight tendency toward α-helicity. Interestingly, some of these fragments can be identified as containing hydrophobic clusters, shown in Figure 4b, and correlate well with the sequence-based predictions of α-helix formation for fragments L130−S135 and I168−F175 (*30*).

Experimental NMR Relaxation Rates. To ascertain further the extent of local motions, a set of relaxation measurements was performed. The NMR relaxation rates R_1 and R_2, and the $\{^1H\}-^{15}N$ NOE values, are sensitive to the backbone motions on the picosecond to nanosecond time scale. In addition, R_2 is influenced by motions on the microsecond to millisecond time scale, which originate mainly from conformational or chemical exchange processes. Thus, the analysis of R_1, R_2, and $\{^1H\}-^{15}N$ NOE constants for backbone amide nitrogen provides information about the backbone dynamics on both the picosecond to nanosecond and microsecond to millisecond time scales (*29*).

Despite poor chemical shift dispersion in the $^1H-^{15}N$ HSQC spectra, a total of 120 cross-peaks of 174 assigned non-prolyl residues were well-resolved, and 107 of them were of sufficient intensity that they could be used for relaxation measurements. The ^{15}N relaxation measurements were carried out at two temperatures, 7 and 27 °C. Figure 5a shows steady-state heteronuclear NOE intensities as a function of residue number. The NOE intensities have a flat profile, with the vast majority of NOE values being positive with mean values of 0.2−0.5. These values are significantly lower than expected for a folded protein. For comparison, residues involved in α-helix or β-strand structural motifs in folded proteins of a size comparable to BG21 have NOE values larger than 0.6, whereas those in relatively flexible loops and turns have positive values smaller than 0.6 (*70*). The reduced NOE values measured in rmBG21 indicate much less restricted dynamics on the picosecond to nanosecond time scale, which is consistent with general lack of ordered secondary structure in rmBG21, as evident also from the CSI analysis. In particular, the residues around Q52−D60 and A125−G128 show much lower NOE values of ∼0.2, indicating that these fragments experience less restricted motions. Interestingly, although all NOE values are lower than those typically measured in folded proteins, they are all positive, indicating that the dynamic motions are more restricted than in a "canonical" IDP (*29*).

The R_1 measurements (not shown) show a featureless profile with relaxation rates ranging from 1.5 to 2.7 s^{-1}, with an average around 2 s^{-1}. The R_1 values generally found for folded proteins of similar size are in the range 1.0−1.2 s^{-1} (*70*), which suggests an increase in the overall tumbling of rmBG21 compared to folded proteins. The R_2 values shown in Figure 5b are much more sequence-dependent and range from 5 to 13 s^{-1}. In particular, the R_2 values for the residues from D65 to R185 are quite dispersed and generally higher, indicating some degree of nonrandom structure in this fragment. However, there is one notable exception, the fragment A125−S135, where R_2 values exhibit a well-pronounced minimum and are consistent with the NOE data that also show a minimum here. This fragment has a high proportion of residues with short side chains, A125, A126, S127, G128, and G129, and the motions of these residues are less sterically constrained. It has been noted previously that motifs rich in Gly and Ala may exhibit extra flexibility due to their small side chain size and may serve as molecular hinges in protein folding (*71*). By contrast, lower and much less dispersed R_2 values are observed here for the N-terminus of rmBG21, indicating increased flexibility in the first 65 residues and a much higher degree of structural randomness. This result also correlates with the lower NOE values for the N-terminal end.

To check if a certain degree of restriction of dynamic motion persists at elevated temperatures, the relaxation measurements were repeated at 27 °C. Figure 6 shows the R_1, R_2, and NOE data recorded at that temperature. Overall, the R_2 values at 27 °C are lower for the entire protein, indicating overall increased flexibility. In agreement with our measurements at 7 °C, the N-terminus (G1−D65) and the Ala/Gly-rich fragment A125−L130 have lower R_2 values. This result correlates well with the significantly negative NOE values for these fragments. In particular, the N-terminal portion of the protein contains two fragments encompassing residues E8−E40 and G46−D65, which become much more mobile. The corresponding NOE values are in the range −0.16 to −0.76 with a mean of −0.37 for E8−E40 and in the range −0.18 to −1.1 with a mean of −0.41 for G46−T69. These figures are comparable to the NOE values measured for other IDPs, which range from −0.4 to −1.2, depending on the size and restriction of motion due to clustering and/or position along the sequence (*29*, *72*).

Further examination of Figure 6 shows that most of the residues between N74 and R185 have positive NOE values, indicating that this part of the protein is less mobile on a picosecond to nanosecond time scale, compared to most of its N-terminal part. The only exception is again the small fragment of residues A125−L130, where significantly negative NOE values are observed. In addition to having a large proportion of glycines and alanines, this highly flexible fragment also occurs at the end of the last Golli-specific fragment preceding the classic MBP, which comprises the residues starting from M133, excluding the C-terminal LEH_6 tag.

Spectral Density Function. The three relaxation parameters, R_1, R_2, and NOE are determined by the spectral density function $J(\omega)$ (*73*):

$$R_1 = (d^2/4)[J(\omega_H - \omega_N) + 3J(\omega_N) + 6J(\omega_H + \omega_N)] + c^2 J(\omega_N) \quad (3)$$

$$R_2 = (d^2/8)[4J(0) + J(\omega_H - \omega_N) + 3J(\omega_N) + 6J(\omega_H) + 6J(\omega_H + \omega_N)] + (c^2/6)[4J(0) + 3J(\omega_N)] + R_{ex} \quad (4)$$

$$\mathrm{NOE} = 1 + (d^2/4R_1)(\gamma_N/\gamma_H)[6J(\omega_H + \omega_N) - J(\omega_H - \omega_N)] \quad (5)$$

where $d = (\mu_0 h \gamma_N \gamma_H / 8\pi^2)\langle r_{NH}^{-3}\rangle$, $c = \omega_N \Delta\sigma/(3)^{1/2}$, μ_0 is the permeability of free space, h is Planck's constant, γ_H and γ_N are gyromagnetic ratios of hydrogen and nitrogen nuclei,

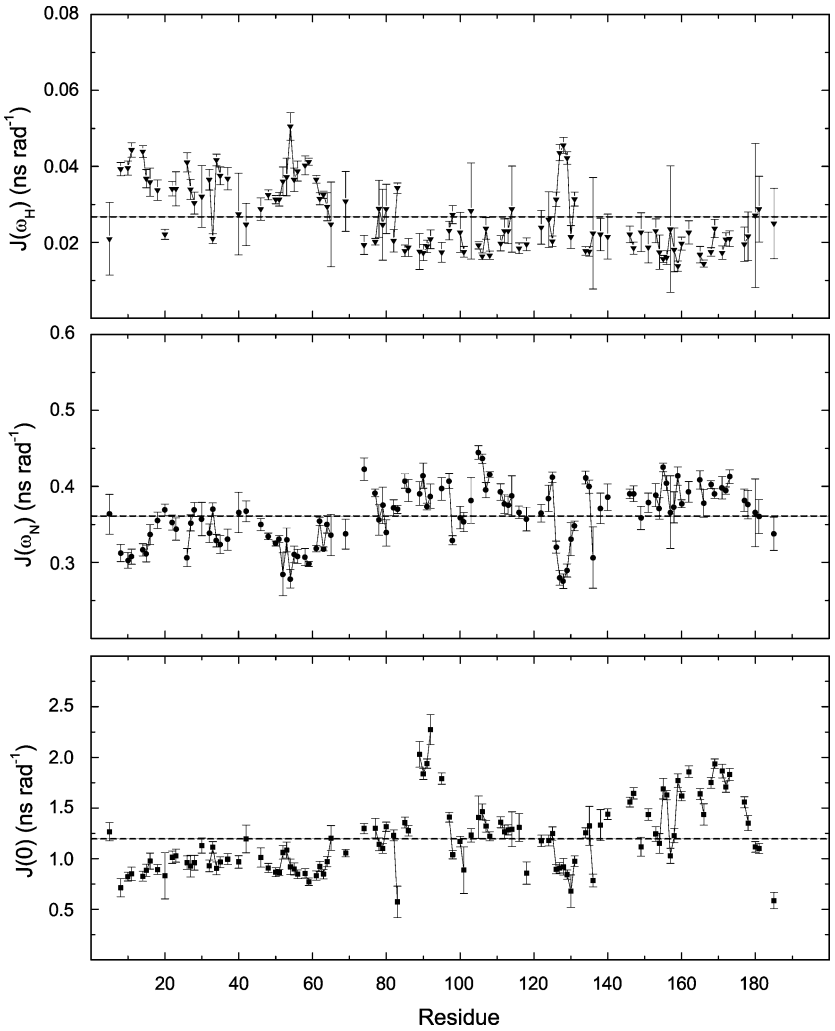

FIGURE 7: Spectral density function at 27 °C, derived at frequencies of 0, 60.8 MHz (ω_N), and 600.1 MHz (ω_H). Reference lines are the mean values of each of the spectral density functions.

respectively, r_{NH} is the proton−nitrogen bond length, ω_H and ω_N are the Larmor frequencies for the proton and nitrogen nuclei, respectively, and $\Delta\sigma$ is the chemical shift anisotropy of ^{15}N (−160 ppm). Here, R_{ex} is a term introduced to account for contributions arising from conformational averaging on the microsecond to millisecond time scale that are not averaged by the CPMG (*53*) pulse train.

The three experimental parameters R_1, R_2, and NOE are not sufficient to extract the spectral density function, $J(\omega)$, at five frequencies. However, the values of $J(\omega_H)$, $J(\omega_H + \omega_N)$, and $J(\omega_H - \omega_N)$ can be assumed to be approximately equal in the case of ^{15}N relaxation (*74*−*76*). Furthermore, assuming that the contribution from slow conformational exchange, R_{ex}, is negligible, then eqs 3−5 can be solved for the spectral density function:

$$J(\omega_H) = 0.2R_1(\text{NOE} - 1)(4/d^2)(\gamma_N/\gamma_H) \quad (6)$$

$$J(\omega_N) = 4R_1/(3d^2 + 4c^2)[1 - (7/5)(\text{NOE} - 1)(\gamma_N/\gamma_H)] \quad (7)$$

$$J(0) = 1/(3d^2 + 4c^2)[6R_2 - 3R_1 - (18R_1/5)(\text{NOE} - 1)(\gamma_N/\gamma_H)] \quad (8)$$

In order to derive the values of the spectral density functions at the three given frequencies, the R_1, R_2, and NOE values measured at 27 °C and the ^1H frequency of 600.13 MHz were used as input parameters for equations (*6*−*8*). The uncertainties of these inputs have been combined using the standard error propagation methods to propagate the uncertainties in the calculated spectral density values.

The average values for $J(0)$, $J(\omega_N)$, $J(\omega_H)$ and the standard deviations are shown in Figure 7, as a function of residue number. The magnitude of the spectral density function at the three frequencies reports on the extent of the NH bond vector motions: in the situation of restricted motions, the most significant contribution will be from the low-frequency component $J(0)$, whereas in the opposite case of high mobility, the high-frequency component $J(\omega_H)$ is expected to be the major contributor. From Figure 7, the values of the high-frequency component are higher than average for the N-terminal domain of rmBG21 and have especially pronounced maxima for G5−G18 and N53−D65. Another local maximum is observed for the flexible fragment A125−A134. This result is accompanied by lower than average values of $J(0)$ observed for the same fragments, indicating that these segments of the protein undergo extensive motions. On the other hand, for residues D65−Q120 and S135−R180, there are lower than average values of $J(\omega_H)$ and higher than average values of $J(0)$, indicating that these segments of rmBG21 have more restricted motions. Two additional noteworthy features in the $J(0)$ plot in Figure 7 are a well

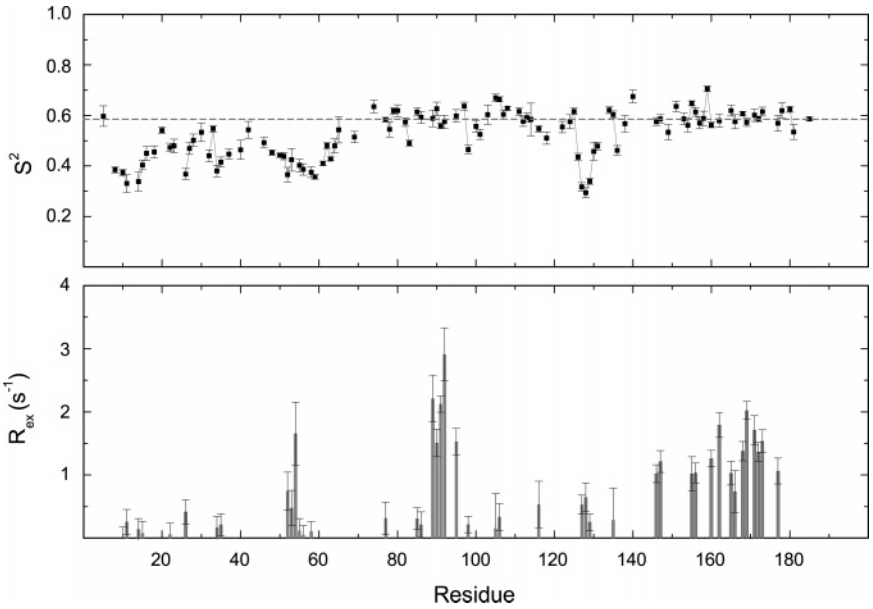

FIGURE 8: MODELFREE results for rmBG21. (a) S^2 and (b) R_{ex} values determined from Lipari−Szabo model-free analysis with the extension of Clore et al., using the globally optimized correlation time of 3.82 ± 0.02 ns. All errors were determined on the basis of 1000 Monte Carlo simulations of Brent's implementation of Powel's method for multidimensional minimization, as described in the MODELFREE manual (*79*, *80*).

pronounced maximum for residues R87−R92 and higher than average values for residues S135−R180, which are signs of restricted low-frequency motions. At the same time, the values for the spectral density function $J(\omega_N)$ lack any notable features for these residues. Thus, the fragments R87−R92 and S135−R180 are subjected to motions on the microsecond to millisecond time scale, probably due to conformational exchange.

Model-Free Analysis and Order Parameter. To quantify the local motions further, and to extract microscopic motional parameters from the amide ^{15}N relaxation rates R_1, R_2, and $\{^1H\}-^{15}N$ NOE, a Lipari−Szabo (*28*, *77*) analysis with the extension of Clore et al. (*78*) was performed with the software MODELFREE (version 4.20) (*79*, *80*). Briefly, the spectral density function, $J(\omega)$, is assumed to be related to a set of motional parameters such as the correlation times and order parameters:

$$J(\omega) = \frac{2}{5}\left[\frac{S^2\tau_m}{1+(\omega\tau_m)^2} + \frac{S_f^2(1-S_s^2)\tau'_s}{1+(\omega\tau'_s)^2} + \frac{(1-S_f^2)\tau'_f}{1+(\omega\tau'_f)^2}\right] \quad (9)$$

where $\tau'_f = \tau_f\tau_m/(\tau_f + \tau_m)$, $\tau'_s = \tau_s\tau_m/(\tau_s + \tau_m)$, τ_m is the overall rotational correlation time of the molecule, τ_f and τ_s are the effective correlation times for internal motions on fast and slow time scales, respectively, and S_f^2, S_s^2, and $S^2 = S_f^2S_s^2$ are the squares of the parameters describing the amplitudes of fast, slow, and generalized motions, respectively.

An initial estimate for the total correlation time τ_m was obtained using the MODELFREE built-in grid search option. Different rotational diffusion models were evaluated, and the isotropic diffusion model was found to provide the best fit to the rmBG21 NMR relaxation data. For the final analysis of the local motions, a total correlation time of 3.81 ns (±0.02 ns) was used. To fit different possible time scale motions, which arise due to structural variations and any consequent motion restrictions and/or exchange (*81*, *82*), the models describing local motions of individual NH vectors were optimized separately. The model selection strategy of Mandel et al. (*80*) was used in order to get the model that best describes the experimental relaxation data. A maximum of three motional parameters, in addition to the overall rotational correlation time, could be fit to the three available relaxation parameters measured at a single static magnetic field strength. Figure 8a shows the optimized order generalized parameter S^2, which describes the motional restriction of the $^{15}N-^1H$ bond vector on the picosecond to nanosecond time scale. The value of S^2 is close to 0.6 for most of the residues. The most disordered part of the protein is found for segments S5−D65 and A126−G129, which have significantly smaller S^2 values in the range of 0.3−0.5.

The presence of low-frequency motions for some fragments is evident from the $J(0)$ plot and has been discussed above. The R_{ex} parameter was introduced to account for these effects. Figure 8b shows the plot of the R_{ex} values extracted from the experimental data using MODELFREE analysis. Whereas S^2 provides a measure of rapid internal motions relative to the overall rotational diffusion, significantly large values of R_{ex} identify residues that experience conformational or chemical exchange on a microsecond to millisecond time scale. It has previously been observed that important biological and biochemical events such as ligand-binding and dissociation rates, and rates of conformational exchange, often occur near that slow time scale (*83*). Therefore, it is possible that the observation of these slower motions for specific residues reflects their functional activity (*84*−*88*). Here, ten residues were observed to have significant R_{ex} values (>1.5 s^{-1}), with the highest values associated with residues H89−R92. These residues are part of a sequence P88−R96 that has the maximum change in amino acid buried area upon folding (data given in the Supporting Information). The significant R_{ex} values, along with the absence of any cooperative secondary chemical shift deviations in this region, might be indicative of conformational exchange

between two states, one being collapsed into a hydrophobic cluster and the other a random coil. The same conclusion might be drawn for most of the C-terminal residues scattered along the segment T151−G173. Tables containing the results of fittings, including extracted parameters, confidence intervals, and the description of models used for fitting relaxation data for a particular residue, are also given in the Supporting Information.

Comparison with Other Intrinsically Disordered Proteins. It is instructive to compare rmBG21 to other intrinsically disordered proteins. In particular, spectral assignments of NMR resonances have recently been obtained for the recombinant murine classic 18.5 kDa isoform of myelin basic protein (rmMBP, BMRB entry 15131) (*89*). This isoform is a peripheral membrane protein whose main function is maintenance of the stability of the myelin sheath but which also polymerizes actin and tubulin in a Ca^{2+}-calmodulin-dependent manner, indicating diverse functionality. Both rmBG21 and rmMBP have a segment in common, encoded by exon 5 (using murine Golli exon numbering, exon Ibc in classic numbering), that comprises the C-terminal residues A134−K189 in rmBG21 and the N-terminal A1−K56 residues in 18.5 kDa MBP. Overall, this fragment is largely disordered in both proteins, and the chemical shifts agree very well for most of these residues (the C^{α} and C^{β} chemical shift differences do not exceed ±0.75 and ±0.4 ppm, respectively). This close agreement indicates that the conformation of this segment in either protein is not affected by the other domains. Studies of 18.5 kDa classic MBP using site-directed spin labeling and electron paramagnetic resonance spectroscopy have shown this segment to be relatively deeply embedded in the lipid bilayer, especially at the position of the FF pair (*90*). At present, BG21 has not yet been demonstrated to be associated with lipids in vivo.

The NMR structural analyses described here also compare interestingly with the demonstration by Reyes and Campagnoni, by site-directed mutagenesis and deletion analyses, that the Golli and classic domains play different roles in the cell (*91*). They have shown that sequences in the MBP domain target the protein into the nucleus, particularly the 36-residue segment (A134−L169 as seen in the BG21 sequence in Figure 2b), and that sequences within the Golli domain induce membrane process sheet extension in OLs and neurons. The mechanism of this posttranslational sorting by which this classic MBP segment of BG21 is used as a nontraditional sorting signal for its translocation to the nucleus may involve some membrane interaction and has not yet been determined.

Another worthwhile example for comparison with BG21 is the transcriptional activation domain (TAD) of human p53, a small regulatory region that initiates DNA transcription (*92*). The TAD of p53 is known to be inherently devoid of tertiary structure due to the net negative charge resulting from the high content of acidic amino acids, such as Asp and Glu (*93*). On the other hand, short p53 TAD fragments are able to form helices upon binding to target proteins (*94*, *95*). In their study on the p53 TAD, Lee et al. (*92*) utilized heteronuclear multidimensional NMR spectroscopy to delineate the details of its local structural elements in its free state and to compare it to the target-bound state. They were able to show that unbound full-length p53 TAD contains a preexisting amphipathic α-helix and two nascent turns. The preexisting α-helix was found to be identical to the α-helix found in the target-bound state, indicating that the structural transition in p53 upon target binding is not a coil-to-helix type but would just involve tightening of the preexisting α-helix into a stable α-helix. On the other hand, studies on fragments of p53 TAD showed that induced α-helices were formed upon target binding, but not in the free state, indicating that the formation of the α-helix is context-dependent. The secondary structure elements found in this study are thought to constitute determinants that act as "hydrophobic antennae," which may facilitate TAD-target recognition and become more structured in the course of target binding. For the case of BG21, such a phenomenon may define its interaction with GIP.

CONCLUDING REMARKS

All of the NMR measurements carried out in this study, and our previous fluorescence and CD spectroscopic measurements (*30*), show that rmBG21 is predominantly disordered in aqueous solution. Here, R_2 and NOE measurements further reveal that the protein can be divided into two regions that exhibit very different dynamic behavior. Most of the residues in the first N-terminal 65 amino acids have significantly negative heteronuclear NOE values and are in general more mobile than the remainder of the protein, which is subjected to much more restricted internal motions. The only exception is a Gly/Ala-rich fragment A125−G130, where significant unrestricted motions are also present. Why are these regions more mobile than the rest of the protein? The increased mobility of the A125−G130 segment is not surprising and is consistent with the hypothesis of Schwarzinger et al. that regions rich in glycines and alanines may serve as molecular hinges in protein folding pathways (*71*). Close investigation of the amino acid sequence of the first 65 N-terminal residues reveals that it is on average more (negatively) charged (mean net charge is −0.062) compared to the entire protein (mean net charge is −0.005); its low mean hydrophobicity (0.3542) is comparable to that of the entire protein (0.366). [The mean net charge and mean hydrophobicity were evaluated using the sequence analysis tools of the EXPASY Proteomics Server (http://expasy.org/) following the method of Uversky et al. (*20*).] Thus, electrostatic interactions may contribute to the increased mobility of the fragment. We can hypothesize at this point that the highly flexible N-terminal third of BG21 provides additional plasticity necessary for effective interactions with other proteins such as GIP. The flexible Gly/Ala region may serve as a molecular hinge in the process of subsequent folding.

ACKNOWLEDGMENT

We are grateful to Drs. Anthony and Celia Campagnoni (Neuropsychiatric Institute, University of California at Los Angeles) for providing the rmBG21 clone, to Mr. D. S. Libich of the University of Guelph for advice on protein purification and NMR spectral processing and analysis software, and to Ms. Valerie Robertson of the University of Guelph NMR Centre for assistance.

SUPPORTING INFORMATION AVAILABLE

Tables containing the detailed acquisition parameters for the acquired spectra, mathematical expressions of the five

different motional models of the extended model-free approach, and the extracted order parameters along with a figure showing secondary structure and hydrophobic cluster analysis. This material is available free of charge via the Internet at http://pubs.acs.org.

REFERENCES

1. Harauz, G., Ishiyama, N., Hill, C. M. D., Bates, I. R., Libich, D. S., and Fares, C. (2004) Myelin basic protein−diverse conformational states of an intrinsically unstructured protein and its roles in myelin assembly and multiple sclerosis, *Micron 35*, 503−542.
2. Campagnoni, A. T., Pribyl, T. M., Campagnoni, C. W., Kampf, K., Amurumarjee, S., Landry, C. F., Handley, V. W., Newman, S. L., Garbay, B., and Kitamura, K. (1993) Structure and developmental regulation of Golli-MBP, a 105-kilobase gene that encompasses the myelin basic-protein gene and is expressed in cells in the oligodendrocyte lineage in the brain, *J. Biol. Chem. 268*, 4930−4938.
3. Feng, J. M., Fernandes, A. O., Campagnoni, C. W., Hu, Y. H., and Campagnoni, A. T. (2004) The golli-myelin basic protein negatively regulates signal transduction in T lymphocytes, *J. Neuroimmunol. 152*, 57−66.
4. Martin, D., Peppler, M. S., and Brodeur, B. R. (1992) Immunological characterization of the lipooligosaccharide-B band of *Bordetella pertussis*, *Infect. Immun. 60*, 2718−2725.
5. Voskuhl, R. R. (1998) Myelin protein expression in lymphoid tissues: implications for peripheral tolerance, *Immunol. Rev. 164*, 81−92.
6. Huseby, E. S., and Goverman, J. (2000) Tolerating the nervous system: A delicate balance, *J. Exp. Med. 191*, 757−760.
7. Campagnoni, A., and Skoff, R. P. (2001) The pathobiology of myelin mutants reveal novel biological functions of the MBP and PLP genes, *Brain Pathol. 11*, 74−91.
8. Feng, J. M., Givogri, I. M., Bongarzone, E. R., Campagnoni, C., Jacobs, E., Handley, V. W., Schonmann, V., and Campagnoni, A. T. (2000) Thymocytes express the golli products of the myelin basic protein gene and levels of expression are stage dependent, *J. Immunol. 165*, 5443−5450.
9. Feng, J. M., Givogri, I. M., Bongarzone, E. R., Campagnoni, C., Jacobs, E., Handley, V., Schonmann, V., and Campagnoni, A. T. (2000) Golli-myelin basic protein expression in thymic cells: Expression in developing thymocytes, *FASEB J. 14*, A1121−A1121.
10. Landry, C. F., Ellison, J., Skinner, E., and Campagnoni, A. T. (1997) Golli-MBP proteins mark the earliest stages of fiber extension and terminal arboration in the mouse peripheral nervous system, *J. Neurosci. Res. 50*, 265−271.
11. Tosic, M., Rakic, S., Matthieu, J. M., and Zecevic, N. (2002) Identification of Golli and myelin basic proteins in human brain during early development, *Glia 37*, 219−228.
12. Filipovic, R., Rakic, S., and Zecevic, N. (2002) Expression of Golli proteins in adult human brain and multiple sclerosis lesions, *J. Neuroimmunol. 127*, 1−12.
13. Filipovic, R., and Zecevic, N. (2005) Interaction between microglia and oligodendrocyte cell progenitors involves Golli proteins, *Biophysics from Molecules to Brain: In Memory of Radoslav K. Andjus 1048*, 166−174.
14. Feng, J. M., Hu, Y. H. K., Xie, L. H., Colwell, C. S., Shao, X. S. M., Sun, X. P., Chen, B. M., Tang, H. Z., and Campagnoni, A. T. (2006) Golli protein negatively regulates store depletion-induced calcium influx in T cells, *Immunity 24*, 717−727.
15. Jacobs, E. C., Pribyl, T. M., Kampf, K., Campagnoni, C., Colwell, C. S., Reyes, S. D., Martin, M., Handley, V., Hiltner, T. D., Readhead, C., Jacobs, R. E., Messing, A., Fisher, R. S., and Campagnoni, A. T. (2005) Region-specific myelin pathology in mice lacking the Golli products of the myelin basic protein gene, *J. Neurosci. 25*, 7004−7013.
16. Feng, J. M., Fernandes, A. O., and Campagnoni, A. T. (2002) Golli-myelin basic proteins delineate the nerve distribution of lymphoid organs, *J. Neuroimmunol. 123*, 1−8.
17. Fernandes, A. O., Campagnoni, C. W., Kampf, K., Feng, J. M., Handley, V. W., Schonmann, V., Bongarzone, E. R., Reyes, S., and Campagnoni, A. T. (2004) Identification of a protein that interacts with the Golli-myelin basic protein and with nuclear-LIM interactor in the nervous system, *J. Neurosci. Res. 75*, 461−471.
18. Yeo, M., Lin, P. S., Dahmus, M. E., and Gill, G. N. (2003) A novel RNA polymerase IIC-terminal domain phosphatase that preferentially dephosphorylates serine 5, *J. Biol. Chem. 278*, 26078−26085.
19. Yeo, M., Lee, S. K., Lee, B., Ruiz, E. C., Pfaff, S. L., and Gill, G. N. (2005) Small CTD phosphatases function in silencing neuronal gene expression, *Science 307*, 596−600.
20. Uversky, V. N., Gillespie, J. R., and Fink, A. L. (2000) Why are "natively unfolded" proteins unstructured under physiologic conditions?, *Proteins: Struct., Funct., Genet. 41*, 415−427.
21. Bhalla, J., Storchan, G. B., MacCarthy, C. M., Uversky, V. N., and Tcherkasskaya, O. (2006) Local flexibility in molecular function paradigm, *Mol. Cell. Proteomics 5*, 1212−1223.
22. Patil, A., and Nakamura, H. (2006) Disordered domains and high surface charge confer hubs with the ability to interact with multiple proteins in interaction networks, *FEBS Lett. 580*, 2041−2045.
23. Dyson, H. J., and Wright, P. E. (2005) Elucidation of the protein folding landscape by NMR, *Methods Enzymol.*: *Nucl. Magn. Reson. Biol. Macromol. 394* (Part C), 299−321.
24. Dyson, H. J., and Wright, P. E. (2006) According to current textbooks, a well-defined three-dimensional structure is a prerequisite for the function of a protein. Is this correct?, *IUBMB Life 58*, 107−109.
25. Dyson, H. J., and Wright, P. E. (2001) Nuclear magnetic resonance methods for elucidation of structure and dynamics in disordered states, *Nucl. Magn. Reson. Biol. Macromol. 339* (Part B), 258−270.
26. Spera, S., and Bax, A. (1991) Empirical correlation between protein backbone conformation and C-alpha and C-beta C-13 nuclear-magnetic-resonance chemical-shifts, *J. Am. Chem. Soc. 113*, 5490−5492.
27. Wishart, D. S., and Sykes, B. D. (1994) Chemical-shifts as a tool for structure determination, *Nucl. Magn. Reson. 239* (Part C), 363−392.
28. Lipari, G., and Szabo, A. (1982) Model-free approach to the interpretation of nuclear magnetic-resonance relaxation in macromolecules. 1. Theory and range of validity, *J. Am. Chem. Soc. 104*, 4546−4559.
29. Shojania, S., and O'Neil, J. D. (2006) HIV-1 Tat is a natively unfolded protein−The solution conformation and dynamics of reduced HIV-1 Tat-(1−72) by NMR spectroscopy, *J. Biol. Chem. 281*, 8347−8356.
30. Bamm, V. V., Ahmed, M. A. M., Ladizhansky, V., and Harauz, G. (2007) Purification and spectroscopic characterization of the recombinant BG21 isoform of murine golli myelin basic protein, *J. Neurosci. Res. 85*, 272−284.
31. Grzesiek, S., and Bax, A. (1992) Improved 3D triple-resonance NMR techniques applied to a 31-kDa protein, *J. Magn. Reson. 96*, 432−440.
32. Kay, L. E., Xu, G. Y., and Yamazaki, T. (1994) Enhanced-sensitivity triple-resonance spectroscopy with minimal H_2O saturation, *J. Magn. Reson., Ser. A 109*, 129−133.
33. Schleucher, J., Sattler, M., and Griesinger, C. (1993) Coherence selection by gradients without signal attenuation−application to the 3-dimensional HNCO experiment, *Angew. Chem., Int. Ed. Engl. 32*, 1489−1491.
34. Clubb, R. T., Thanabal, V., and Wagner, G. (1992) A constant-time 3-dimensional triple-resonance pulse scheme to correlate intraresidue H-1(N), N-15, and C-13(′) chemical-shifts in N-15-C-13-labeled proteins, *J. Magn. Reson. 97*, 213−217.
35. Muhandiram, D. R., and Kay, L. E. (1994) Gradient-enhanced triple-resonance 3-dimensional NMR experiments with improved sensitivity, *J. Magn. Reson., Ser. B 103*, 203−216.
36. Wittekind, M., and Mueller, L. (1993) HNCACB, a high-sensitivity 3D NMR experiment to correlate amide-proton and nitrogen resonances with the alpha-carbon and beta-carbon resonances in proteins, *J. Magn. Reson., Ser. B 101*, 201−205.
37. Grzesiek, S., and Bax, A. (1993) Amino-acid type determination in the sequential assignment procedure of uniformly C-13/N-15-enriched proteins, *J. Biomol. NMR 3*, 185−204.
38. Kanelis, V., Donaldson, L., Muhandiram, D. R., Rotin, D., Forman-Kay, J. D., and Kay, L. E. (2000) Sequential assignment of proline-rich regions in proteins: Application to modular binding domain complexes, *J. Biomol. NMR 16*, 253−259.
39. Wang, A. C., Grzesiek, S., Tschudin, R., Lodi, P. J., and Bax, A. (1995) Sequential backbone assignment of isotopically enriched proteins in D_2O by deuterium-decoupled HA(CA)N and HA(CACO)N, *J. Biomol. NMR 5*, 376−382.

40. Delaglio, F., Grzesiek, S., Vuister, G. W., Zhu, G., Pfeifer, J., and Bax, A. (1995) NMRPipe—a multidimensional spectral processing system based on unix pipes, *J. Biomol. NMR 6*, 277−293.
41. Markley, J. L., Bax, A., Arata, Y., Hilbers, C. W., Kaptein, R., Sykes, B. D., Wright, P. E., and Wuthrich, K. (1998) Recommendations for the presentation of NMR structures of proteins and nucleic acids, *J. Mol. Biol. 280*, 933−952 [reprinted from (1998) *Pure Appl. Chem. 70*, 117−142].
42. Cavanagh, J., Fairbrother, W. J., Palmer, A. G., and Skelton, N. J. (1996) *Protein NMR spectroscopy—principles and practice*, Academic Press, San Diego.
43. Palmer, A. G., Cavanagh, J., Wright, P. E., and Rance, M. (1991) Sensitivity improvement in proton-detected 2-dimensional heteronuclear correlation NMR-spectroscopy, *J. Magn. Reson. 93*, 151−170.
44. Kay, L., Keifer, P., and Saarinen, T. (1992) Pure absorption gradient enhanced heteronuclear single quantum correlation spectroscopy with improved sensitivity, *J. Am. Chem. Soc. 114*, 10663−10665.
45. Schleucher, J., Schwendinger, M., Sattler, M., Schmidt, P., Schedletzky, O., Glaser, S. J., Sorensen, O. W., and Griesinger, C. (1994) A general enhancement scheme in heteronuclear multidimensional NMR employing pulsed-field gradients, *J. Biomol. NMR 4*, 301−306.
46. Keller, R. (2004) *The computer aided resonance assignment tutorial*, 1st ed., Cantina Verlag, Goldau, Switzerland.
47. Masse, J. E., and Keller, R. (2005) AutoLink: Automated sequential resonance assignment of biopolymers from NMR data by relative-hypothesis-prioritization-based simulated logic, *J. Magn. Reson. 174*, 133−151.
48. Wang, Y. J., and Jardetzky, O. (2002) Probability-based protein secondary structure identification using combined NMR chemical-shift data, *Protein Sci. 11*, 852−861.
49. Schwarzinger, S., Kroon, G. J. A., Foss, T. R., Chung, J., Wright, P. E., and Dyson, H. J. (2001) Sequence-dependent correction of random coil NMR chemical shifts, *J. Am. Chem. Soc. 123*, 2970−2978.
50. Palmer, A. G., Skelton, N. J., Chazin, W. J., Wright, P. E., and Rance, M. (1992) Suppression of the effects of cross-correlation between dipolar and anisotropic chemical-shift relaxation mechanisms in the measurement of spin-spin relaxation rates, *Mol. Phys. 75*, 699−711.
51. Kay, L. E., Torchia, D. A., and Bax, A. (1989) Backbone dynamics of proteins as studied by N-15 inverse detected heteronuclear NMR-spectroscopy—Application to staphylococcal nuclease, *Biochemistry 28*, 8972−8979.
52. Boyd, J., Hommel, U., and Campbell, I. D. (1990) Influence of cross-correlation between dipolar and anisotropic chemical shift relaxation mechanisms upon longitudinal relaxation rates of ^{15}N in macromolecules, *Chem. Phys. Lett. 175*, 477−482.
53. Meiboom, S., and Gill, D. (1958) Modified spin-echo method for measuring nuclear relaxation times, *Rev. Sci. Instrum. 29*, 688−691.
54. Libich, D. S., Robertson, V. J., Monette, M. M., and Harauz, G. (2004) Backbone resonance assignments of the 18.5 kDa isoform of murine myelin basic protein (MBP), *J. Biomol. NMR 29*, 545−546.
55. Yao, J., Dyson, H. J., and Wright, P. E. (1997) Chemical shift dispersion and secondary structure prediction in unfolded and partly folded proteins, *FEBS Lett. 419*, 285−289.
56. Wüthrich, K. (1986) *NMR of Proteins and Nucleic Acids*, Wiley, New York.
57. Yao, J., Chung, J., Eliezer, D., Wright, P. E., and Dyson, H. J. (2001) NMR structural and dynamic characterization of the acid-unfolded state of apomyoglobin provides insights into the early events in protein folding, *Biochemistry 40*, 3561−3571.
58. Uversky, V. N., Li, J., and Fink, A. L. (2001) Evidence for a partially folded intermediate in alpha-synuclein fibril formation, *J. Biol. Chem. 276*, 10737−10744.
59. Permyakov, S. E., Millett, I. S., Doniach, S., Permyakov, E. A., and Uversky, V. N. (2003) Natively unfolded C-terminal domain of caldesmon remains substantially unstructured after the effective binding to calmodulin, *Proteins: Struct., Funct., Genet. 53*, 855−862.
60. Uversky, V. N. (2002) What does it mean to be natively unfolded?, *Eur. J. Biochem. 269*, 2−12.
61. Uversky, V. N. (2002) Natively unfolded proteins: A point where biology waits for physics, *Protein Sci. 11*, 739−756.
62. Uversky, V. N., Permyakov, S. E., Zagranichny, V. E., Rodionov, I. L., Fink, A. L., Cherskaya, A. M., Wasserman, L. A., and Permyakov, E. A. (2002) Effect of zinc and temperature on the conformation of the gamma subunit of retinal phosphodiesterase: A natively unfolded protein, *J. Proteome Res. 1*, 149−159.
63. Timm, D. E., Vissavajjhala, P., Ross, A. H., and Neet, K. E. (1992) Spectroscopic and chemical studies of the interaction between nerve growth-factor (NGF) and the extracellular domain of the low affinity NGF receptor, *Protein Sci. 1*, 1023−1031.
64. Kim, T. D., Ryu, H. J., Cho, H. I., Yang, C. H., and Kim, J. (2000) Thermal behavior of proteins: Heat-resistant proteins and their heat-induced secondary structural changes, *Biochemistry 39*, 14839−14846.
65. Matthew, J. B., and Richards, F. M. (1983) The pH-dependence of hydrogen exchange in proteins, *J. Biol. Chem. 258*, 3039−3044.
66. Ro, H. A., and Carson, J. H. (2004) pH microdomains in oligodendrocytes, *J. Biol. Chem. 279*, 37115−37123.
67. Peti, W., Smith, L. J., Redfield, C., and Schwalbe, H. (2001) Chemical shifts in denatured proteins: Resonance assignments for denatured ubiquitin and comparisons with other denatured proteins, *J. Biomol. NMR 19*, 153−165.
68. Wishart, D. S., and Sykes, B. D. (1994) The C-13 chemical-shift Index—A simple method for the identification of protein secondary structure using C-13 chemical-shift data, *J. Biomol. NMR 4*, 171−180.
69. Lin, K., Simossis, V. A., Taylor, W. R., and Heringa, J. (2005) A simple and fast secondary structure prediction method using hidden neural networks, *Bioinformatics 21*, 152−159.
70. Coles, M., Diercks, T., Muehlenweg, B., Bartsch, S., Zolzer, V., Tschesche, H., and Kessler, H. (1999) The solution structure and dynamics of human neutrophil gelatinase-associated lipocalin, *J. Mol. Biol. 289*, 139−157.
71. Schwarzinger, S., Wright, P. E., and Dyson, H. J. (2002) Molecular hinges in protein folding: the urea-denatured state of apomyoglobin, *Biochemistry 41*, 12681−12686.
72. Donne, D. G., Viles, J. H., Groth, D., Mehlhorn, I., James, T. L., Cohen, F. E., Prusiner, S. B., Wright, P. E., and Dyson, H. J. (1997) Structure of the recombinant full-length hamster prion protein PrP(29−231): The N terminus is highly flexible, *Proc. Natl. Acad. Sci. U.S.A. 94*, 13452−13457.
73. Abragam, A. (1961) *Principles of Nuclear Magnetism*, Clarendon Press, Oxford.
74. Peng, J. W., and Wagner, G. (1992) Mapping of the spectral densities of N-H bond motions in eglin-C using heteronuclear relaxation experiments, *Biochemistry 31*, 8571−8586.
75. Ishima, R., and Nagayama, K. (1995) Protein backbone dynamics revealed by quasi spectral density-function analysis of amide N-15 nuclei, *Biochemistry 34*, 3162−3171.
76. Farrow, N. A., Zhang, O. W., Forman-Kay, J. D., and Kay, L. E. (1995) Comparison of the backbone dynamics of a folded and an unfolded SH3 domain existing in equilibrium in aqueous buffer, *Biochemistry 34*, 868−878.
77. Lipari, G., and Szabo, A. (1982) Model-free approach to the interpretation of nuclear magnetic-resonance relaxation in macromolecules. 2. Analysis of experimental results, *J. Am. Chem. Soc. 104*, 4559−4570.
78. Clore, G. M., Szabo, A., Bax, A., Kay, L. E., Driscoll, P. C., and Gronenborn, A. M. (1990) Deviations from the simple 2-parameter model-free approach to the interpretation of N-15 nuclear magnetic-relaxation of proteins, *J. Am. Chem. Soc. 112*, 4989−4991.
79. Palmer, A. G., Rance, M., and Wright, P. E. (1991) Intramolecular motions of a zinc finger DNA-binding domain from xfin characterized by proton-detected natural abundance C-12 heteronuclear NMR-spectroscopy, *J. Am. Chem. Soc. 113*, 4371−4380.
80. Mandel, A. M., Akke, M., and Palmer, A. G. (1995) Backbone dynamics of *Escherichia-coli* ribonuclease HI—correlations with structure and function in an active enzyme, *J. Mol. Biol. 246*, 144−163.
81. Alexandrescu, A. T., and Shortle, D. (1994) Backbone dynamics of a highly disordered 131-residue fragment of staphylococcal nuclease, *J. Mol. Biol. 242*, 527−546.
82. Buck, M., Schwalbe, H., and Dobson, C. M. (1996) Main-chain dynamics of a partially folded protein: N-15 NMR relaxation measurements of hen egg white lysozyme denatured in trifluoroethanol, *J. Mol. Biol. 257*, 669−683.
83. Mukherjee, M., Dutta, K., White, M. A., Cowburn, D., and Fox, R. O. (2006) NMR solution structure and backbone dynamics of

domain III of the E protein of tick-borne Langat flavivirus suggests a potential site for molecular recognition, *Protein Sci. 15*, 1342−1355.

84. Epstein, D. M., Benkovic, S. J., and Wright, P. E. (1995) Dynamics of the dihydrofolate-reductase folate complex—Catalytic sites and regions known to undergo conformational change exhibit diverse dynamical features, *Biochemistry 34*, 11037−11048.
85. Kristensen, S. M., Siegal, G., Sankar, A., and Driscoll, P. C. (2000) Backbone dynamics of the C-terminal SH2 domain of the p85 alpha subunit of phosphoinositide 3-kinase: Effect of phosphotyrosine-peptide binding and characterization of slow conformational exchange processes, *J. Mol. Biol. 299*, 771−788.
86. McCoy, M. A., Senior, M. M., Gesell, J. J., Ramanathan, L., and Wyss, D. F. (2001) Solution structure and dynamics of the single-chain hepatitis C virus NS3 protease NS4A cofactor complex, *J. Mol. Biol. 305*, 1099−1110.
87. Dutta, K., Shi, H. H., Cruz-Chu, E. R., Kami, K., and Ghose, R. (2004) Dynamic influences on a high-affinity, high-specificity interaction involving the C-terminal SH3 domain of P67(phox), *Biochemistry 43*, 8094−8106.
88. Palmer, A. G. (2004) NMR characterization of the dynamics of biomacromolecules, *Chem. Rev. 104*, 3623−3640.
89. Libich, D. S., Monette, M. M., Robertson, V. J., and Harauz, G. (2007) NMR assignment of an intrinsically disordered protein under physiological conditions: the 18.5 kDa isoform of murine myelin basic protein, *Biomol. NMR Assignments* (in press) (doi 10.1007/s12104-007-9016-1).
90. Bates, I. R., Boggs, J. M., Feix, J. B., and Harauz, G. (2003) Membrane-anchoring and charge effects in the interaction of myelin basic protein with lipid bilayers studied by site-directed spin labeling, *J. Biol. Chem. 278*, 29041−29047.
91. Reyes, S. D., and Campagnoni, A. T. (2002) Two separate domains in the golli myelin basic proteins are responsible for nuclear targeting and process extension in transfected cells, *J. Neurosci. Res. 69*, 587−596.
92. Lee, H., Mok, K. H., Muhandiram, R., Park, K. H., Suk, J. E., Kim, D. H., Chang, J., Sung, Y. C., Choi, K. Y., and Han, K. H. (2000) Local structural elements in the mostly unstructured transcriptional activation domain of human p53, *J. Biol. Chem. 275*, 29426−29432.
93. Fields, S., and Jang, S. K. (1990) Presence of a potent transcription activating sequence in the p53 protein, *Science 249*, 1046−1049.
94. Uesugi, M., and Verdine, G. L. (1999) The alpha-helical FXXPhi Phi motif in p53: TAF interaction and discrimination by MDM2, *Proc. Natl. Acad. Sci. U.S.A. 96*, 14801−14806.
95. Blommers, M. J. J., Fendrich, G., GarciaEcheverria, C., and Chene, P. (1997) On the interaction between p53 and MDM2: Transfer NOE study of a p53-derived peptide ligated to MDM2, *J. Am. Chem. Soc. 119*, 3425−3426.

BI700632X